STRUCTURAL BIOLOGY

Structural basis of plp2-mediated cytoskeletal protein folding by TRiC/CCT

Wenyu Han[1,2], Mingliang Jin[1]†, Caixuan Liu[1], Qiaoyu Zhao[1,2], Shutian Wang[1], Yifan Wang[1], Yue Yin[3], Chao Peng[3], Yanxing Wang[1], Yao Cong[1,2]*

The cytoskeletal proteins tubulin and actin are the obligate substrates of TCP-1 ring complex/Chaperonin containing TCP-1 (TRiC/CCT), and their folding involves co-chaperone. Through cryo–electron microscopy analysis, we present a more complete picture of TRiC-assisted tubulin/actin folding along TRiC adenosine triphosphatase cycle, under the coordination of co-chaperone plp2. In the open S1/S2 states, plp2 and tubulin/actin engaged within opposite TRiC chambers. Notably, we captured an unprecedented TRiC-plp2-tubulin complex in the closed S3 state, engaged with a folded full-length β-tubulin and loaded with a guanosine triphosphate, and a plp2 occupying opposite rings. Another closed S4 state revealed an actin in the intermediate folding state and a plp2. Accompanying TRiC ring closure, plp2 translocation could coordinate substrate translocation on the CCT6 hemisphere, facilitating substrate stabilization and folding. Our findings reveal the folding mechanism of the major cytoskeletal proteins tubulin/actin under the coordination of the biogenesis machinery TRiC and plp2 and extend our understanding of the links between cytoskeletal proteostasis and related human diseases.

INTRODUCTION

The eukaryotic group II chaperonin TRiC/CCT assists the folding of about 10% of cytosolic proteins, including many key structural and regulatory proteins. TRiC plays an essential role in maintaining cellular protein homeostasis, and dysfunction of TRiC is closely related to cancer and neurodegenerative diseases (*1*–*3*). The key cytoskeletal proteins actin and tubulin, the most abundant and highly conserved proteins in eukaryotic cells, are obligate substrates of TRiC (*4*–*7*). This chaperonin is also essential for the folding of cell cycle regulator CDC20 (*8*) and many proteins involved in oncogenesis, such as p53, VHL tumor suppressor, and STAT3 (signal transducer and activator of transcription 3) (*9*–*11*). TRiC undergoes large conformational changes to encapsulate and release bound substrate proteins during its adenosine triphosphate (ATP)–dependent folding cycle (*12*–*14*).

TRiC is the most complex chaperonin system, consisting of two octameric rings stacked back-to-back. Each ring of TRiC encompasses eight paralogous subunits, CCT1 to CCT8 (sharing ~23 to 35% sequence identity for yeast TRiC), arranged in a specific order (*15*–*20*). Consistent with this specific order, TRiC displays subunit specificity in ATP consumption, ring closure, and substrate recognition and folding (*15*, *18*, *21*). Each TRiC subunit consists of an equatorial domain (E domain) that contains the ATP-binding site and forms intra- and inter-ring contacts, an apical domain (A domain) that comprises interaction sites with target proteins, and an intermediate domain (I domain) that connects the E and A domains (*22*–*24*).

The filament-forming actin and tubulin are abundant cytoskeletal proteins that support diverse cellular processes. Owing to the unique properties of these proteins, a notably complex cellular machinery consisting minimally of the chaperonin TRiC, prefoldin (PFD), phosducin-like proteins (PhLPs), and tubulin cofactors has evolved to facilitate their biogenesis (fig. S1) (*25*). TRiC cooperates with co-chaperone PFD in the folding of actins and tubulins (*26*, *27*); in this process, PFD stabilizes substrate proteins and delivers them to the open TRiC cavity (*25*, *26*, *28*–*31*). Three homologous families of PhLPs (PhLP1, PhLP2, and PhLP3) have been identified, and these proteins each feature an N-terminal helical domain, a central thioredoxin fold domain (TRDX domain), and a C-terminal extension (*32*, *33*). PhLP2 has been shown to be essential for ciliogenesis and microtubule assembly (*34*, *35*), and temperature-sensitive alleles of plp2, the homolog of PhLP2 in *Saccharomyces cerevisiae*, have been shown to cause defects in TRiC-mediated actin and tubulin functions (*35*). Mammalian PhLP2A modulates the TRiC chaperonin activity during folding of cytoskeletal proteins, and yeast plp2 yields a considerably higher actin folding rate than does assisted by TRiC alone (*36*–*38*). It has been indicated that the ciliary precursor tubulin needs to be folded by TRiC with the assistance of PhLP2 (*34*). On the basis of previous structural studies on TRiC-actin and TRiC-tubulin complexes at intermediate or relatively low resolutions (*6*, *7*, *39*–*42*), a recent study reported cryo–electron microscopy (cryo-EM) structures of human TRiC-PhLP2A-actin and TRiC-tubulin complexes both in the closed state at near-atomic resolution and in an open TRiC structure with potential substrate density located in the inter-ring septum (*43*). Still, how PhLP2 coordinates with the TRiC-assisted folding of actin and especially of tubulin in the ATP-driven TRiC conformational cycle needs to be further investigated.

In the present study, we determined an ensemble of cryo-EM structures of *S. cerevisiae* TRiC along its adenosine triphosphatase (ATPase) cycle, with simultaneously engaged plp2 and substrate actin or tubulin inside its chamber, one per ring, in the resolution

[1]State Key Laboratory of Molecular Biology, National Center for Protein Science Shanghai, Shanghai Institute of Biochemistry and Cell Biology, Center for Excellence in Molecular Cell Science, Chinese Academy of Sciences, Shanghai 200031, China. [2]University of Chinese Academy of Sciences, Beijing 100049, China. [3]National Facility for Protein Science in Shanghai, Zhangjiang Lab, Shanghai Advanced Research Institute, CAS, Shanghai 201210, China.
†Present address: University of California San Francisco, San Francisco, CA 94143-0244, USA.
*Corresponding author. Email: cong@sibcb.ac.cn

range of 3.05 to 4.55 Å. In the open S1 and S2 states, we observed plp2, with the detectable TRDX domain, contacting the CCT3/1/4 subunits of TRiC and the substrate density in the opposite ring mostly located in the CCT6 hemisphere (containing CCT1/3/6/8 subunits). Our structural analyses further revealed the upward translocations of both plp2 and substrates with TRiC ring closure, as well as the molecular details of the unique TRiC-plp2 interaction mode. Notably, we captured the TRiC-plp2-tubulin tertiary complex, with tubulin having reached the fully folded state and loaded with a guanosine triphosphate (GTP) since its "birth" from the TRiC chamber, not observed previously to the best of our knowledge. Collectively, our study suggested that plp2 serves as a co-chaperone of TRiC-assisted substrate tubulin/actin folding and revealed a stepwise substrate folding process within the TRiC chamber accompanying its ATP-driven conformational cycle, providing mechanistic insights into how plp2 participates in the substrate tubulin/actin folding process assisted by TRiC.

RESULTS

Simultaneous binding of plp2 and substrates inside an open-state TRiC chamber

To capture a complete picture of TRiC-assisted substrate folding and to reveal the role of plp2 in this process, we purified *S. cerevisiae* TRiC, plp2, and actin (fig. S2A). We then incubated them together without adding nucleotide, and they were confirmed to form a complex according to a native gel analysis (fig. S2B). Our mass spectrometry (MS) results further suggested the co-presence of TRiC with actin and plp2, in addition to endogenous yeast β-tubulin, which was co-purified with TRiC from yeast in a lesser amount (table S2). Here, we followed a previous report to pretreat actin and plp2 with EDTA, which can unfold actin (*37*). Under this condition, actin was unfolded while plp2 was not, according to a thermostability assay (fig. S2, C to F).

Our cryo-EM study on this system produced a map of an open-state TRiC loaded with two extra pieces of density inside its chamber, one in each ring, at a resolution of 4.55 Å (termed S1 state; Fig. 1, A and B; fig. S3, A to C; and table S1). The two pieces of density appeared distinct (Fig. 1B). Overall, the TRiC conformation was observed to be comparable to our previous yeast TRiC structure in the nucleotide partially preloaded (NPP) state (fig. S3D) (*18*), both displaying the following characteristic features: (i) CCT1 being the most outward tilted subunit (Fig. 1A), a feature common in yeast, bovine, and human open-state TRiC (*12*, *18*, *39*, *44*); (ii) the A and I domains of CCT2 as a whole displaying a bent feature (Fig. 1A), unique for the yeast TRiC-NPP state (*18*); and (iii) CCT7 also being slightly outward tilted (fig. S3D). These features allowed us to assign the TRiC subunits and build an atomic model for the S1 map (fig. S3E). In this map, CCT3/6/8 subunits also bore preloaded nucleotides as in the substrate-free TRiC-NPP map (fig. S3F) (*18*). Collectively, these data indicated the S1 TRiC to be in the NPP state.

Further inspection of the S1 map revealed that, in the cis-ring chamber, the extra density was attached to the consecutive CCT3/1/4 subunits, including the respective A domains of CCT3/4 and E domains of CCT3/1 (Fig. 1C). To better distinguish the different rings of TRiC, we defined the plp2-occupied chamber as the "cis-ring" and the substrate-occupied chamber as the "trans-ring," and these definitions are followed throughout the manuscript. The lower portion of the extra density matched well with the TRDX domain of yeast plp2 (Fig. 1E), indicating that the cis-ring extra density most likely corresponded to plp2. Corroborative to this, our chemical cross-linking and MS (XL-MS) analysis also detected XLs between plp2 and CCT3/1/4 (Fig. 1G and table S3). Regarding the extra density in the trans-ring chamber, this density was observed to be adjacent to the CCT8/6/3 subunits, involving the respective A domains of CCT6/3 and E domains of all three subunits (Fig. 1D). Still, this extra density was less well resolved (Fig. 1F), and whether it corresponded to actin, tubulin, or even another plp2 was difficult to determine. Moreover, our XL-MS analysis revealed an XL between actin and CCT6 (Fig. 1, D and G, and table S3). Combined with our MS result indicating the co-presence of endogenous tubulin with TRiC, although in a lesser amount (table S2), and the distinct shape and location of the extra density in the trans-ring, we postulated that the trans-ring extra density may have corresponded to dynamic forms of bound substrates actin and tubulin in their initial stages of folding. Therefore, analysis of our S1 map suggested that, in the open NPP state, yeast TRiC can simultaneously engage with plp2 in one ring and the essential cytoskeletal proteins actin or tubulin in the opposite ring. This arrangement is distinct from that in the recent open-state human TRiC structure, with potential substrate (tubulin/actin) density in the inter-ring septum (*43*).

Unchanged location of plp2 after ATP binding to TRiC

To capture a thorough picture of plp2-mediated tubulin/actin folding assisted by TRiC along its ATPase cycle, we incubated the abovementioned system with ATP-AlFx, a nucleotide analog that has been used to mimic the ATP-hydrolysis transition state in previous structural studies on TRiC and TRiC-substrate complexes (*12*, *19*, *28*, *39*, *43*, *45*, *46*). Our cryo-EM study on this system revealed two conformational states of TRiC (fig. S4A), one in the open state and the other in the closed state (discussed later). The open and closed states of TRiC showed a population distribution of 27 and 73%, respectively (fig. S4, A and B), quite distinct from that of our previous substrate-free yeast TRiC in the same chemical condition, in which almost all TRiC complexes were observed in the closed conformation (*19*). Moreover, our NADH (reduced form of nicotinamide adenine dinucleotide)–coupled assay suggested essentially identical ATPase activities of TRiC in the presence and absence of plp2 and actin (fig. S6). Together, the presence of plp2 and actin does not alter the TRiC ATPase activity but instead could tune the allosteric network of TRiC, with 27% of TRiC particles showing a delayed transformation to the closed state (see Discussion).

Further focused classification of the TRiC-open dataset led to an open-state map, with TRiC engaged with two extra pieces of density, one inside each chamber (termed S2 state; Fig. 2, A and B; fig. S4, A, C, and D; and fig. S5, A and B). In the S2 map, each of the TRiC subunits was associated with density that matched ATP reasonably well (fig. S5D). In addition, the overall open TRiC conformation resembled that of TRiC–AMP-PNP (adenylyl-imidodiphosphate) (fig. S5C) (*18*), with the A and I domains of CCT2 unbent and CCT7 tilted inwards, making the complex less asymmetric and stabilized slightly. Together, these data suggested that the S2 map was of TRiC in the ATP-bound state. Further inspection of this map showed the cis-ring extra density adjacent to the respective A domains of CCT3/4 and E domains of CCT3/1, with this density

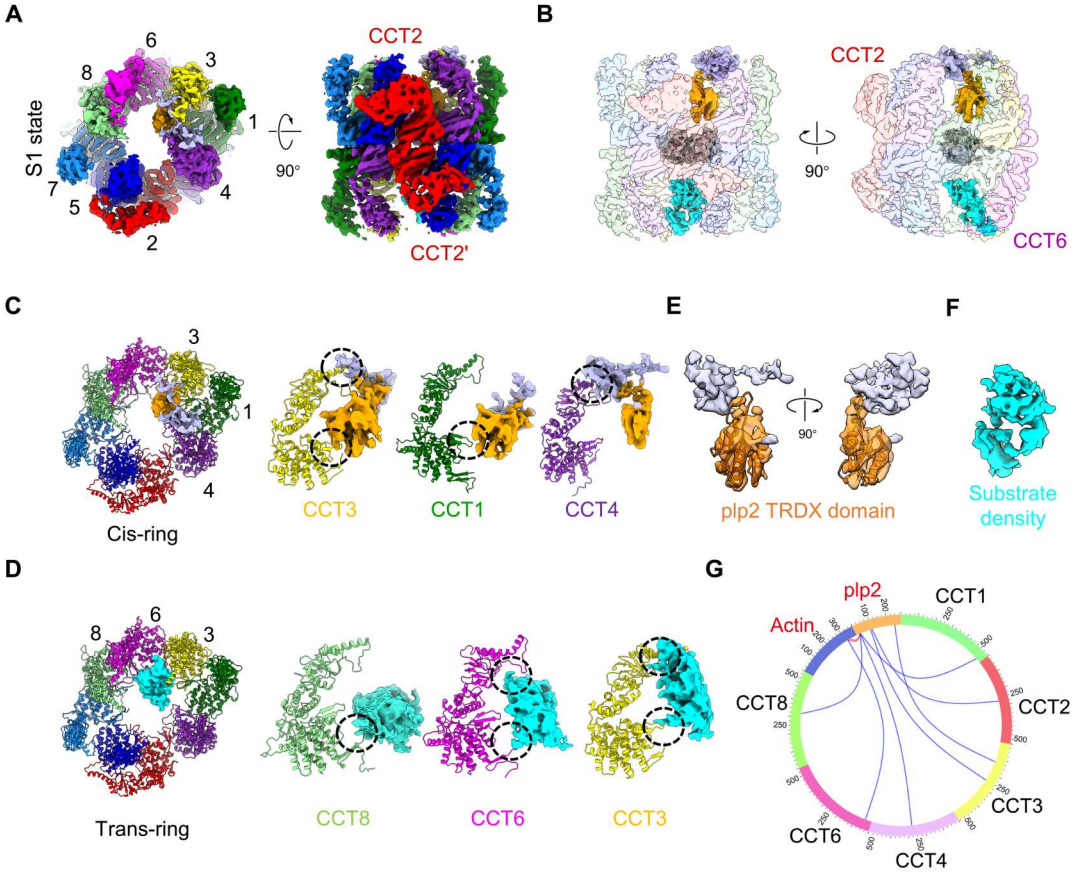

Fig. 1. Cryo-EM structure of the TRiC-plp2-substrate complex showing plp2 and substrate located within a distinct TRiC chamber in the open NPP state. (**A**) Top and side views of the map of the TRiC-plp2-substrate complex in the S1 state, with the different TRiC subunits shown in distinct colors. This subunit color scheme was followed in subsequent figures. (**B**) Side view of an unsharpened S1 map exhibiting the locations of extra densities in the cis- and trans-rings and unstructured tail mass (gray) relative to the TRiC chamber (transparent). (**C**) Top view of the S1 model and side view of related subunits showing the extra density in the cis-ring in contact with the CCT3/1/4 subunits. The contact areas are indicated by black dashed circles. (**D**) Bottom view of the S1 model and side views of related subunits, showing the extra density in the trans-ring in contact with the CCT8/6/3 subunits. (**E**) Visualization of the extra density in the cis-ring, with the lower portion of the density fitted well with the TRDX domain (orange) of plp2, and the rest of the density appearing to correspond to the relatively dynamic N domain (lilac). (**F**) Visualization of the extra density in the trans-ring, with this density showing poor structural features and connectivity. (**G**) Cross-linking and MS (XL-MS) analysis of the TRiC-plp2-substrate complex. Identified cross-linked TRiC-actin/plp2 contacts are shown as blue lines and actin-plp2 contacts as red lines. We used best *e* value (1.00×10^{-2}) as the threshold to remove extra XL-MS data with lower confidence.

matching well the structure of the TRDX domain of plp2 (Fig. 2, C and D), overall similar to the plp2 observed in the S1 map (Fig. 1, C and E). The extra density in the trans-ring appeared distinct in size and shape to that in the cis-ring, and most likely corresponded to tubulin/actin substrate (Fig. 2, E and F). It appeared to form contacts with the CCT3/1/4 subunits, implying a potential substrate translocation upon ATP binding to TRiC. Together, our S1 and S2 maps both suggested that, in either the NPP or the ATP-bound open state of yeast TRiC, plp2 and substrate actin or tubulin can simultaneously occupy TRiC chamber, one per ring, not seen in the open-state human TRiC structure (*43*).

Cooperation of TRiC with plp2 in the folding of tubulin/actin accompanying TRiC ring closure

For the closed-state TRiC dataset of the ATP-AlFx presented sample, we performed further focused three-dimensional (3D) classifications on the inner chamber of each of the two TRiC rings and obtained three cryo-EM maps, termed S3, S4, and S5 states at resolutions of 3.39, 3.20, and 3.05 Å, respectively (fig. S4, A, C, and E). Specifically, each of the S3 and S4 maps showed two extra pieces of density, one inside each chamber, appearing distinct in shape (Figs. 3, A and B, and 4, A and B); while the S5 map showed two almost identical extra pieces of density, one in each ring (Fig. 5, A and B). For the closed-state TRiC maps, a characteristic kink feature in the A domain α-helical protrusion of one subunit (fig. S5E), corresponding to the unique feature of CCT6 (*15*), and a protruding density corresponding to the inserted calmodulin binding protein (CBP)-tag on the A domain of CCT3 were directly visualized (fig. S5F). These characteristics allowed us to identify the subunits and build a model for each of the S3, S4, and S5 maps (fig. S5, G to L).

In the S3 map, the cis-ring extra density was observed to match the plp2 model well, with the TRDX domain and about half of the N-terminal helical domain and C-terminal extension resolved (Fig. 3, C and D). The plp2 density appeared to lie underneath the dome, interacting with the CCT6/3/1/7/5/2 subunits of TRiC

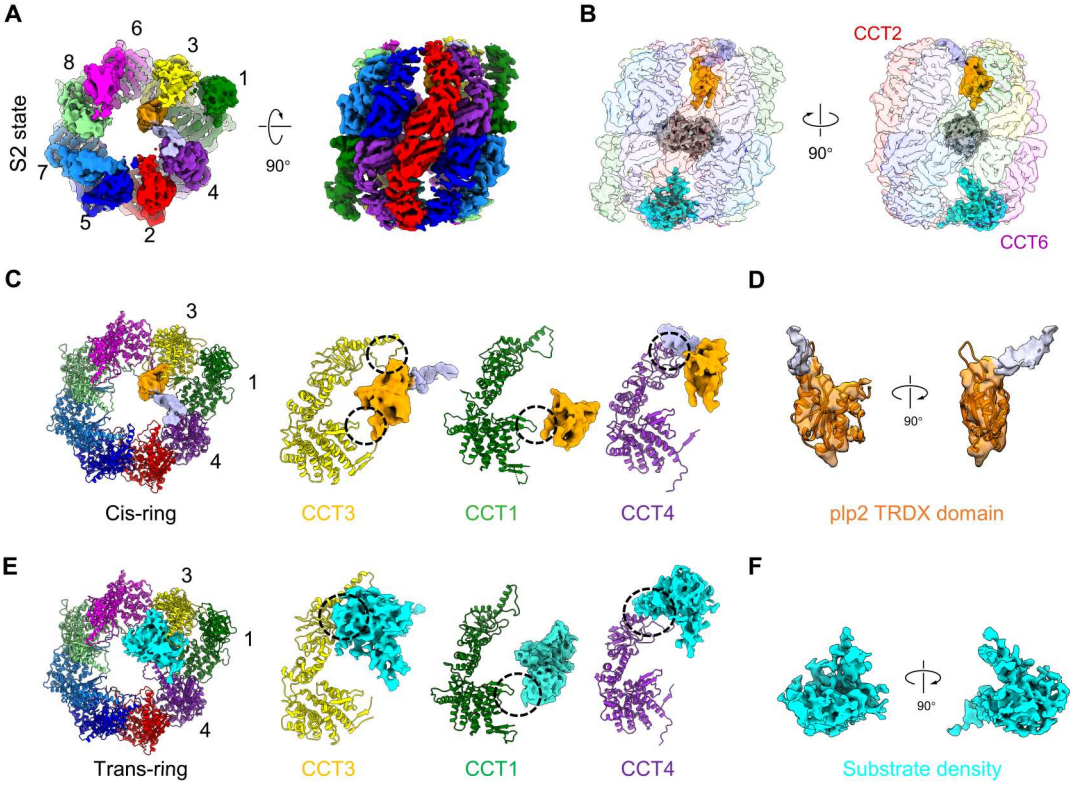

Fig. 2. Cryo-EM structure of the TRiC-plp2-substrate complex in the open S2 state. (**A**) Top and side views of the cryo-EM map of the TRiC-plp2-substrate S2 state with TRiC displaying open ATP-bound conformation. (**B**) Side view of the unsharpened S2 map showing the extra densities in the cis- and trans-ring chambers and unstructured tail mass (gray) relative to the TRiC chamber (transparent). (**C**) Top view of the S2 model and side views of related subunits showing the extra density in the cis-ring in contact with CCT3/1/4 subunits, similar to that in the S1 state. (**D**) Visualization of the cis-ring extra density, also with the lower portion of the density fitted well with the TRDX domain (orange) of plp2, and the rest of the density appearing to correspond to the dynamic N domain (lilac). (**E**) Bottom view of the S2 model and side view of related subunits, showing the extra density in the trans-ring in contact with CCT3/1/4. (**F**) Visualization of the trans-ring extra density in the S2 state, showing poor structural features and connectivity as for S1.

(Fig. 3, B and C; with details of the TRiC-plp2 interactions described below). Collectively, our structures suggested the occurrence, accompanying TRiC ring closure, of a translocation of the plp2 TRDX domain from the CCT6 hemisphere (in the open S1 and S2 states) to the CCT2 hemisphere (containing CCT4/2/5/7 subunits, in the closed S3 state; Figs. 1C, 2C, and 3C). In addition, the trans-ring extra density was found to match the structural features of full-length folded tubulin very well (Fig. 3, C and E to G). Notably, this TRiC-plp2-tubulin ternary structure has not been captured before to the best of our knowledge, although has been detected biochemically (*35*). In conjugation with TRiC ring closure and plp2 translocation, tubulin also shifted upward and appeared stabilized, although it remained on the CCT6 hemisphere as in the open S1/S2 states. In addition, the folded tubulin density exhibited structural features of the S355-A364 loop, usually used to distinguish β-tubulin from α-tubulin (*47*, *48*), and hence confirmed the resolved tubulin to be β-tubulin (Fig. 3, F and H), in line with our MS results (table S2). Unexpectedly, this folded β-tubulin also showed a bound density that matched GTP very well (Fig. 3H), indicating that the newly made β-tubulin was already loaded with a GTP molecule before being released from the TRiC chamber. Inspection of the interaction between TRiC and tubulin revealed that the N-terminal and C-terminal domains of tubulin were attached to the A and E domains of CCT8/6/3/1 subunits, mainly with helix 11 of each of CCT8/6/3, loop^{H11} of each of CCT8/6/3/1, loop^{H10} of CCT6, the protrusion loop of each of CCT8/6/1, and the E domain stem loop of each of the CCT6/3/1 subunits (Fig. 3, I and J; fig. S5N; and table S4). Further inspection of surface properties showed the abovementioned interaction footprint on TRiC to be more positively charged, compensating for the overall negatively charged tubulin in the interaction interface (Fig. 3K) and showed hydrophilic interactions of tubulin with TRiC (Fig. 3L). Collectively, our yeast TRiC-plp2-tubulin structure enabled us to capture unexpected features compared with previous TRiC-tubulin structures (*40*, *43*), including a plp2 molecule present together with tubulin substrate in the TRiC chamber (one per ring), a bound GTP in the newly made β-tubulin, and tubulin fully folded to its native state, whereas the tubulin I domain has been shown to remain disordered in the human TRiC-tubulin structure in the absence of plp2 (*43*). Therefore, the presence of plp2 could play a role in stabilizing and folding the tubulin substrate.

In the S4 map, the cis-ring extra density was also identified as plp2, displaying the same conformation and binding location as in S3 (Fig. 4, C and D, and fig. S5M). The trans-ring extra density mainly occupied the CCT6 hemisphere, as observed in the open S1 and S2 states. This density was found to overall match the actin

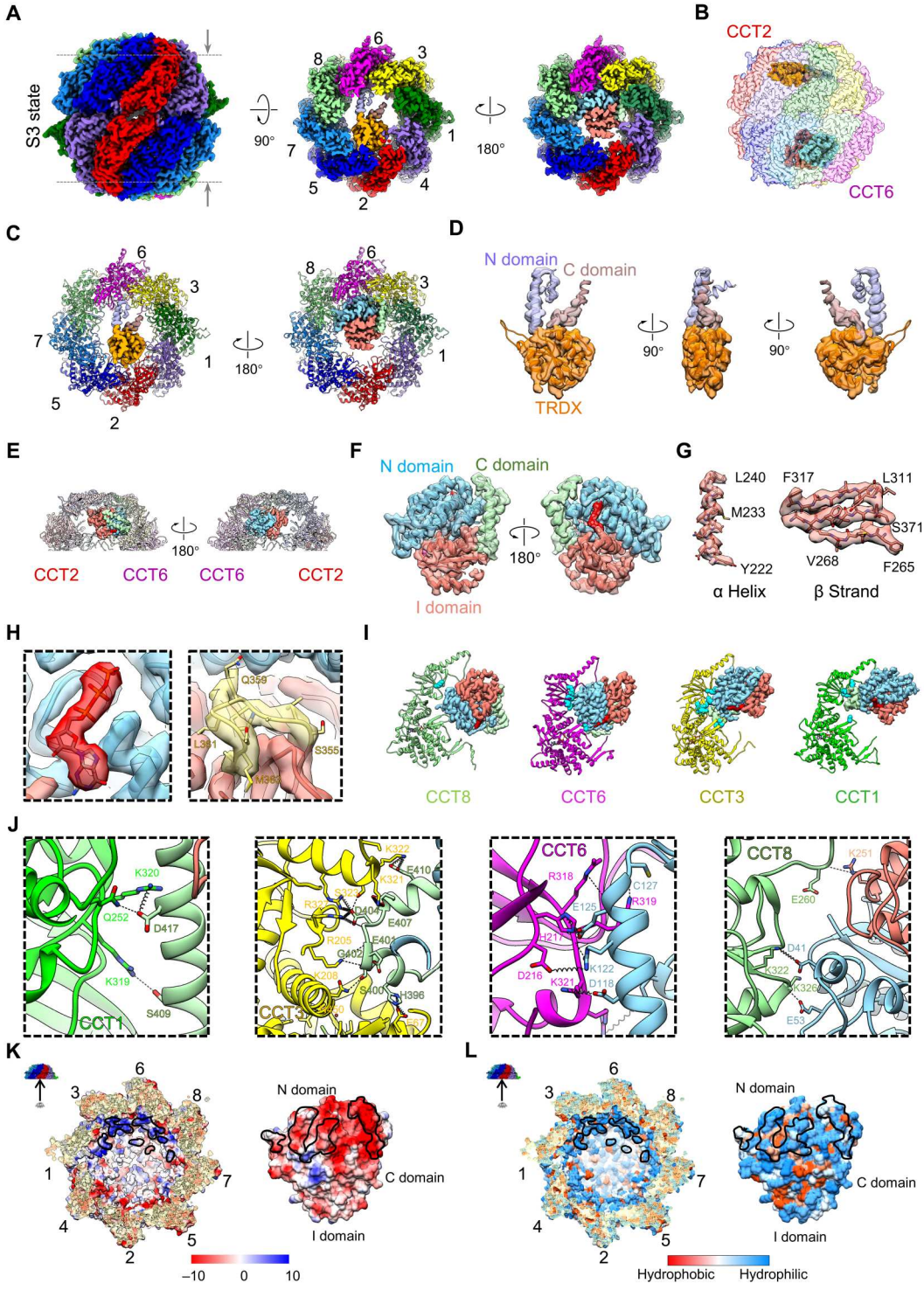

Fig. 3. Cryo-EM structure of the TRiC-plp2-tubulin complex in the closed S3 state, showing simultaneously bound plp2 and a β-tubulin in the native folded state loaded with a GTP. (**A**) Different views of the S3 map. Only the region between the dashed gray lines in the side view image were included in the top and bottom views. (**B**) Side view of the S3 map showing the location of extra pieces of density within the TRiC chamber. (**C**) Top and bottom views showing the extra density in the cis-ring interacting with the CCT6/3/1/2/5/7 subunits and the extra density in the trans-ring interacting with the CCT8/6/3/1 subunits. (**D**) Extra density in the cis-ring of S3 fitted well with the plp2 model. The N-terminal, TRDX, and C-terminal domains of plp2 are shown in lilac, orange, and rosy brown, respectively. This subunit color scheme of plp2 was followed in subsequent figures. (**E**) Different side views showing substrate density in the trans-ring mainly located in the CCT6 hemisphere. (**F**) The trans-ring extra density in S3 fitted well with the β-tubulin model (PDB: 5W3F). The N-terminal, I, and C-terminal domains of tubulin are colored sky blue, salmon, and pale green, respectively. (**G**) High-resolution structural features of the tubulin I domain. (**H**) Magnified views showing the GTP model (red) fitted well into density and the short S355-A364 loop (khaki) used to distinguish β- from α-tubulin. (**I**) TRiC-tubulin interaction interface analysis showing that tubulin attached to the respective A or E domains of CCT8/6/3/1. The amino acid residues of TRiC subunits close to (within 4 Å) tubulin are shown as cyan balls (table S4). (**J**) Structures showing the detailed interaction networks between β-tubulin and TRiC, with dashed black lines representing hydrogen bonds and springs representing salt bridges. (**K** and **L**) Surface property analyses of the TRiC–β-tubulin complex showing β-tubulin interacting with TRiC through electrostatic (K) and hydrophilic (L) interactions.

model although being less well resolved, indicating a relatively dynamic status of actin potentially in an intermediate state of folding (Fig. 4, E and F). Actin appeared to mainly attach to CCT8/6/3/1, with its unstructured portion stretching into the chamber (Fig. 4E). Our S4 map was observed to be overall similar to the recent structure of the human TRiC-actin-PhLP2A complex also in the closed state (*43*), with the actin here more in an intermediate state of folding (see also Discussion).

Interactions between plp2 and closed-state TRiC

Regarding the S5 map resolved at a resolution of 3.05 Å, the plp2 model fit into the extra pieces of density in both rings very well (Fig. 5, C to E, and fig. S4E), indicating that plp2, if at a sufficiently

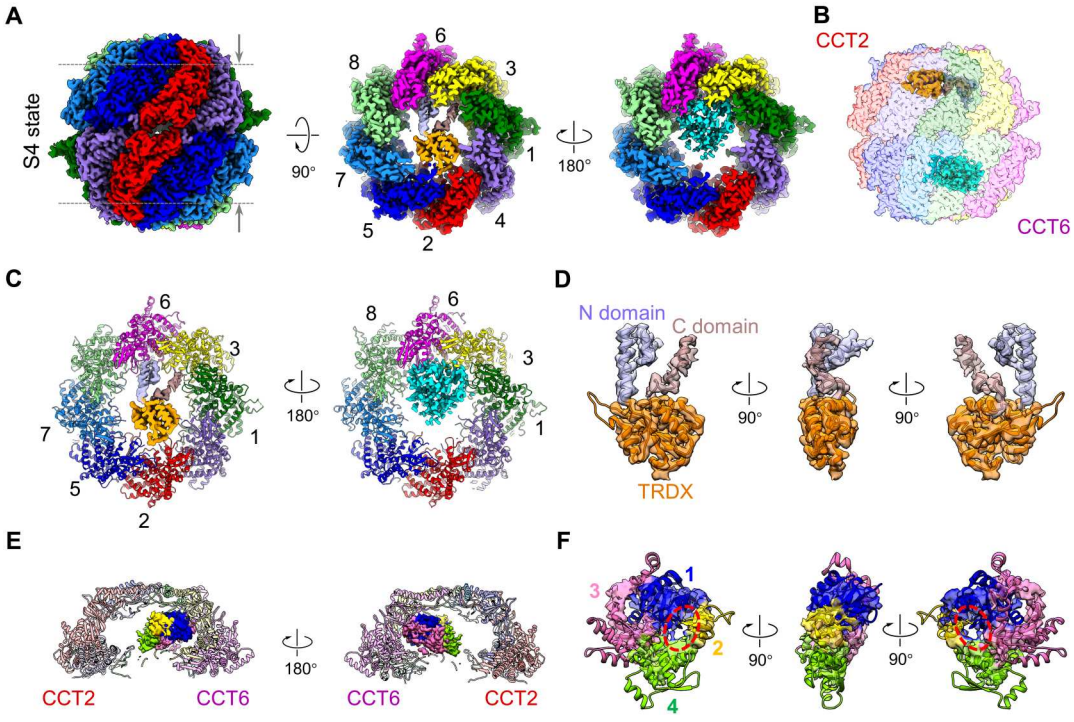

Fig. 4. Cryo-EM structure of the TRiC-plp2-actin complex in the closed S4 state. (**A**) Different views of the closed S4 map. Only the region between the dashed gray lines in the side view image were included in the top and bottom views to better illustrate the extra densities located underneath the dome of TRiC. (**B**) Side view of S4 showing the locations of extra pieces of density within the TRiC chamber. (**C**) Top and bottom views showing that the cis-ring extra density interacted with the CCT6/3/1/2/5/7 subunits and the trans-ring extra density interacted with the CCT8/6/3/1 subunits. (**D**) The extra density in the cis-ring of S4 fitted well with the plp2 model. (**E**) Different side views showing substrate density in the trans-ring mainly located in the CCT6 hemisphere with the weak portion of this density tilted toward the CCT2 hemisphere. (**F**) Rigid body fitting of an actin model (PDB:1YAG) into the trans-ring extra density of the S4 map. Here, subdomains 1 to 4 of actin are colored blue, gold, hot pink, and green, respectively. Red dashed circles indicate the cleft between subdomain 2 and subdomain 4 in native actin.

high concentration, could occupy both chambers of TRiC. Moreover, in the cis-ring of the S3/S4 maps and both rings of the S5 map, the engaged plp2 exhibited similar architectures and orientations within the closed TRiC chamber (fig. S5M); thus, we used the better-resolved cis-ring plp2 in S5 for structural analysis of plp2 with closed TRiC. Here, in addition to the TRDX domain, several α helices of the N-terminal helical domain of plp2 and part of its flexible C-terminal extension were also well resolved (Fig. 5, D and E). Specifically, the N-terminal helical domain and C-terminal extension of plp2 attached to CCT6/3/1 subunits from the CCT6 hemisphere—with the TRDX domain of plp2, originally engaged with CCT3/1/4 subunits in the open S1/S2 states—now translocated and engaged with CCT2/5/7 from the CCT2 hemisphere across the inner chamber (Fig. 5, C and F). Collectively, our data suggested accompanying TRiC ring closure, both plp2 and the cytoskeletal substrates tubulin/actin translocate within the TRiC chamber, with plp2 stretching across the inner chamber of TRiC and, at the same time, tubulin and actin interacting mainly with the CCT6 hemisphere subunits.

Our further structural analysis revealed salt bridges and hydrogen bonds (H bonds) formed mainly between the respective A domains of CCT6/3/1/2/5/7 and the corresponding plp2 structural elements (Fig. 5, F and G, and table S5). Moreover, inspection of the electrostatic interactions between plp2 and TRiC revealed that the more positively charged CCT6 hemisphere is complementary with the plp2 N-terminal helical domain, and the more negatively charged CCT2 hemisphere is complementary with the lower edge of the plp2 TRDX domain (Fig. 5H). In addition, plp2 and TRiC were both observed to display hydrophilic properties in their interaction interface (Fig. 5I). Together, TRiC and plp2 interact through a combination of electrostatic and hydrophilic interactions.

As a control experiment, we performed a further cryo-EM study on the yeast TRiC-actin complex in the presence of ATP-AlFx but in the absence of plp2. No extra density was detected inside the closed TRiC chamber (fig. S7), indicating no engaged substrate in TRiC in the absence of plp2. This result was in line with a previous study on the bovine TRiC-actin complex, which suggested that actin may be very dynamic and cannot be resolved even within the closed TRiC chamber (*39*). Together, plp2 may serve as a co-chaperone facilitating substrate stabilization and folding within the TRiC chamber.

DISCUSSION

Chaperonin TRiC and the PhLPs play critical roles in mediating the biogenesis of the major cytoskeletal proteins actin and tubulin, thus with their activity being linked to any cellular process that depends on the integrity of the microfilament and microtubule-based cytoskeletal systems (*25*, *49*). Still, how PhLP2 coordinates with TRiC in the folding of cytoskeletal proteins, especially tubulin, when accompanying ATP-driven TRiC ring closure needs to be further investigated. In the current work, we present ternary yeast TRiC-plp2-tubulin and TRiC-plp2-actin structures in the closed state (Figs. 3

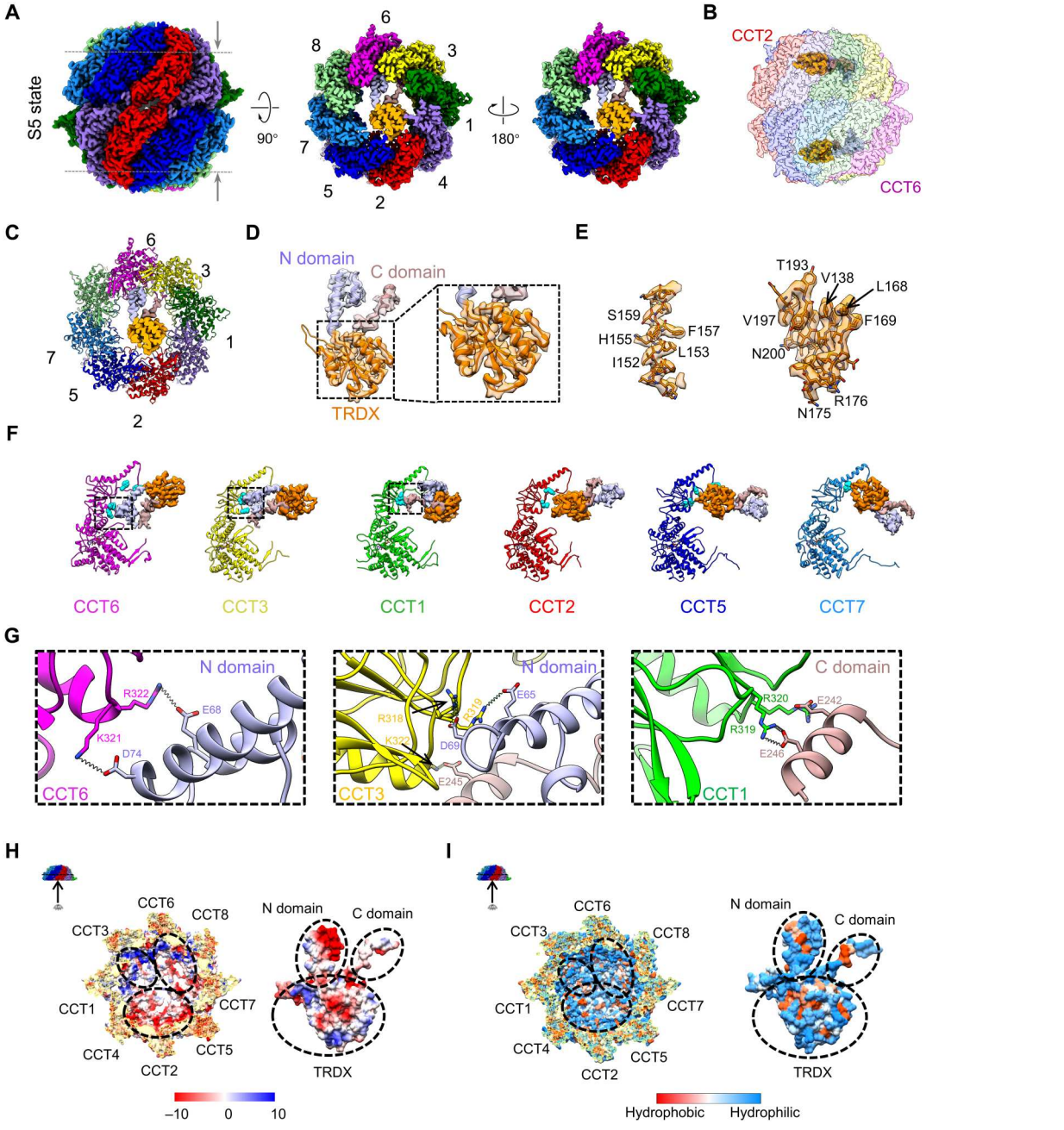

Fig. 5. Mode of interactions between TRiC and plp2 revealed through the closed S5 state. (**A** and **B**) Different views of the closed S5 state map, showing the locations of two identical extra densities within the TRiC chamber. (**C**) Top view showing that plp2 density interacted with the CCT6/3/1/2/5/7 subunits. (**D**) Extra pieces of density in cis- and trans-rings of S5 fitted well with the plp2 model. Here, in addition to the TRDX domain of plp2, several α helices of the N-terminal helix domain of plp2 and part of its flexible C-terminal extension were also well resolved. (**E**) High-resolution structural features of plp2 in S5. (**F**) Interaction interface analysis using protein interactions, surfaces, and assemblies (PISA), showing that plp2 attached to the respective A domains of CCT6/3/1/2/5/7. The residues of TRiC subunits close to (within 4 Å) plp2 are shown as cyan balls (table S5). (**G**) Magnified views of the regions in the black dashed boxes of (F), with springs indicating salt bridges formed between plp2 and CCT6/3/1 subunits. (**H** and **I**) Surface property analysis of the TRiC-plp2 interaction interface, showing plp2 mainly interacting with TRiC through electrostatic (H) and hydrophilic (I) interactions.

and 4), with the former structure not previously reported. We also determined TRiC-plp2-substrate structures in the open NPP (S1) and ATP-bound (S2) states, with plp2 and substrate occupying different chambers in each of these two states (Figs. 1 and 2), distinct from the recent report (*43*). Notably, our TRiC-plp2-tubulin (S3) structure suggested that, with the assistance of plp2, yeast β-tubulin reaches the fully folded state with an ordered I domain and even loaded with a GTP since its birth, i.e., before being released from the TRiC chamber (Fig. 3). Our structural analyses combined with biochemical and MS data provide a more complete picture of the plp2-mediated folding of major cytoskeletal proteins tubulin/actin by TRiC along its conformational cycle and reveal a role of plp2 potentially as a co-chaperone in stabilization and folding of substrates tubulin/actin within the TRiC chamber. Our study sheds light on the structural basis of biogenesis of tubulin and actin mediated by TRiC cooperated with plp2.

Mechanism of plp2- and TRiC-coordinated tubulin/actin folding accompanying TRiC ring closure

On the basis of our results, we put forward a mechanism of plp2-mediated tubulin/actin folding by TRiC accompanying its ATPase cycle (Fig. 6 and movie S1). First, substrate-free NPP state TRiC can spontaneously engage with plp2 and substrate tubulin or actin in its initial folding state, one per ring, forming the S1 state (step 1). In this stage, the plp2 TRDX domain engages with CCT3/1/4 subunits, and substrate mainly interacts with CCT8/6/3 of the CCT6 hemisphere. Subsequently, binding of ATP to TRiC stabilizes TRiC and makes it more symmetrical, while plp2 remains in its original location, forming the S2 state (step 2). Afterward, accompanying TRiC ring closure driven by ATP hydrolysis, both plp2 and substrate tubulin/actin translocate upward to lie underneath the dome, with plp2 stretching across the TRiC chamber, forming S3/S4 states (step 3). With TRiC ring closure, the complex becomes more symmetrical, and the generated mechanical force could assist substrate to overcome the energy barrier toward correct folding. In this state, the substrate, especially tubulin, has been better structured with the assistance of plp2. Eventually, after

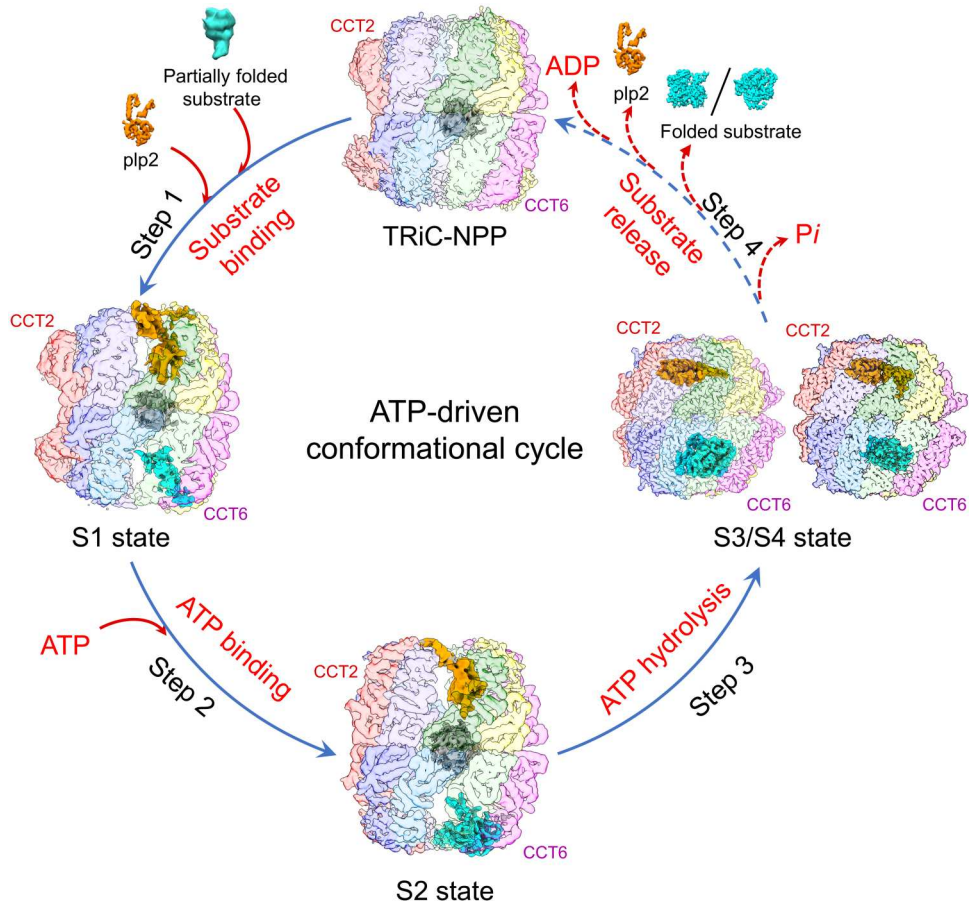

Fig. 6. Proposed TRiC-plp2–mediated tubulin/actin folding process. Co-chaperone plp2 and partially folded substrate tubulin/actin can spontaneously bind open NPP state TRiC within distinct chambers, one per ring, forming the S1 state (step 1). Subsequently, binding of ATP stabilizes TRiC and makes it more symmetrical, while plp2 remains in its original location, forming the S2 state (step 2). Accompanying ATP hydrolysis–driven TRiC ring closure, both plp2 and substrate tubulin/actin translocate upward to lie underneath the dome, with plp2 stretching across the TRiC chamber and substrate transforming toward folded state, forming S3/S4 states (step 3). Upon release of P*i* and reopening of the TRiC chamber, plp2 and the substrate are released from the chamber (step 4), allowing for a new round of substrate folding. ADP, adenosine diphosphate.

TRiC releasing γ-phosphate and reopening its chamber, we postulate that substrate and plp2 could be released from the chamber (step 4). Then, plp2 could be reused by TRiC. A released but not fully folded substrate (such as actin) may need multiple rounds of binding and folding within TRiC to reach its native folded state (*50*).

We found substrate tubulin/actin engaged with the CCT6 hemisphere subunits (CCT8/6/3) in the open S1 (NPP) state (Fig. 1D), and the remaining in the CCT6 hemisphere in the closed S3/S4 states (Figs. 3E and 4E). Consistently, previous studies also suggested a preference for other substrates (including AML1-ETO, Gβ, and mLST8) to bind the CCT6 hemisphere, especially in open-state TRiC (*51*–*53*). We previously showed CCT8/6/3 in the CCT6 hemisphere of NPP state TRiC having preloaded adenosine diphosphate (ADP) from the environment of cells (*18*), which may stabilize these subunits, making them serve as an anchor for substrate engagement. Collectively, the asymmetry or specificity of the TRiC subunits in nucleotide binding may contribute to substrate engagement and processing.

Potential role of plp2 in TRiC-assisted tubulin/actin folding

Our data indicated that, in yeast, plp2 coordinates with TRiC to assist the folding of major cytoskeletal proteins tubulin/actin, with plp2 serving as a co-chaperone. Compared with other co-chaperones, plp2 has been indicated to exhibit a more complex interaction mode with TRiC in the following aspects: (i) plp2 engages with TRiC inside its chamber in both open and closed states (Fig. 6), while other co-chaperones, such as Hsp70, PFD, and PhLP1, usually bind open-state TRiC outside the chamber (*15*, *28*, *33*, *44*, *51*, *54*–*56*); (ii) plp2 and substrate occupy opposite TRiC chambers, instead of in the same ring as in the TRiC-PFD-actin and TRiC-PhLP1-Gβ cases (*44*, *51*); and (iii) plp2 engages with TRiC through a combination of electrostatic and hydrophilic interactions (Fig. 5, H and I), more complex than that of the electrostatic PFD-TRiC interaction (*44*). Along with TRiC ring closure, we captured plp2 translocation within the TRiC chamber coordinating substrate translocation, a feature not reported previously, potentially facilitating substrate stabilization and folding.

In our current work, we also captured the ternary TRiC-plp2-tubulin complex (S3 state), with the full-length β-tubulin in the folded native state even loaded with a GTP molecule (Fig. 3F). However, in the available TRiC-tubulin structures, plp2 was absent and tubulin is either with its I domain missing (*43*) or only partially ordered (*40*). This set of results indicated the role of plp2 as a co-chaperonin in tubulin stabilization and folding. Still, the actin density within TRiC was less well resolved in our S4 map than in the closed human TRiC-actin-PhLP2A structure (*43*), in which actin was stabilized by directly contacting the long helix of the N-terminal domain of PhLP2A, not visualized in our S4 map. Nevertheless, the abovementioned differences could also be attributed to the distinct species, experimental conditions, or substrate folding stages, which need further examination.

We have previously shown almost all TRiC particles appearing in the closed state in the yeast TRiC-ATP-AlFx complex free of substrate and co-chaperone (*19*). Our current structural analysis demonstrated that the presence of plp2 and substrate could change the open-to-closed population ratio of TRiC: In this system, 27% of TRiC particles remained open in the presence of ATP-AlFx (fig. S4, A and B), in line with a recent study on TRiC-PFD-σ3 (*28*). These results collectively indicated that the engagement of plp2 and substrate may slow down TRiC ring closure rate. Moreover, it has been proposed that being less cooperative than attainable allows chaperonins to support robust folding over a wider range of metabolic conditions (*57*, *58*). Together, we postulate that, with the engagement of plp2 and substrate, TRiC could tune its allosteric network to be less cooperative, slowing down its ring closure; in this way, substrate may have a higher chance of being folded into its native state inside a TRiC chamber in a given round of cycling.

In summary, the present study provides a more complete picture of plp2-mediated tubulin and actin folding assisted by TRiC accompanying its ATP-driven conformational cycle. Moreover, our study indicates that, through engagement with TRiC via occupying one chamber throughout its ring closure process, plp2 may be involved in mediating the substrate engagement and stabilization in the opposite TRiC chamber and also in the substrate folding process by adjusting the rate of ring closure of TRiC. Collectively, our data indicate that, in the yeast system, plp2 plays a role as co-chaperone in the TRiC-assisted folding of tubulin/actin. Our findings provide structural insights into the folding mechanism of the major cytoskeletal proteins tubulin/actin under the coordination of the complex biogenesis machinery TRiC and plp2 and could extend our understanding of the links between cytoskeletal proteostasis and human diseases such as developmental and neurological disorders.

MATERIALS AND METHODS

Purification of yeast TRiC

Yeast TRiC was purified according to our published protocol (*18*). The supernatant of yeast lysate was incubated with calmodulin resin (GE Healthcare) overnight at 4°C. Elution of TRiC was achieved using elution buffer [20 mM Hepes (pH 7.5), 5 mM $MgCl_2$, 0.1 mM EDTA, 50 mM NaCl, 1 mM dithiothreitol (DTT), 10% glycerol, and 2 mM EGTA]. The pooled eluate containing TRiC was further purified using size exclusion chromatography (Superose 6 Increase, GE Healthcare) and then concentrated with a Millipore Ultrafree centrifugal filter device (100-kDa cutoff).

Expression and purification of yeast plp2 and actin

The yeast plp2 and actin were cloned into a modified pET28a vector that included a tobacco etch virus (TEV) protease site after the N-terminal 6xHis tag and were expressed in *Escherichia coli* Rosetta (DE3). Plp2 was purified by carrying out a one-step Ni affinity extraction, followed by size exclusion chromatography (Superdex 200, GE Healthcare). Actin was expressed as an inclusion body. The pellet containing inclusion bodies were first denatured using 6 M guanidine hydrochloride and then renatured by dialyzing the resulting mixture in dialysis buffer [25 mM tris-HCl (pH 7.5), 150 mM NaCl, 2 mM $CaCl_2$, and 0.25 mM ATP]. The renaturing supernatant was purified by performing a Ni affinity extraction, followed by size exclusion chromatography (Superdex 200, GE Healthcare).

TRiC-plp2-actin complex formation

To prepare the sample of the TRiC-plp2-actin complex without nucleotide, we diluted the purified yeast TRiC with MQA buffer [20 mM Hepes (pH 7.5), 50 mM NaCl, 5 mM $MgCl_2$, 0.1 mM EDTA, and 1 mM DTT] to 1 μM and then incubated the resulting dilution with plp2 and β-actin, in the presence of 2 mM EDTA at 30°C for 30 min, to have a TRiC–to–plp2–to–β-actin molar ratio of 1:10:10. To

prepare the sample of the TRiC-plp2-actin complex in the presence of 1 mM ATP-AlFx, we further incubated the abovementioned sample with 1 mM ATP, 10 mM $MgCl_2$, 5 mM $Al(NO_3)_3$, and 30 mM NaF at 30°C for 1 hour. The same procedure was applied for producing the TRiC-actin complex with ATP-AlFx.

XL-MS analysis

The TRiC-plp2-actin complex prepared as described above was cross-linked by reacting it with a 2 mM final concentration of bis [sulfosuccinimidyl] suberate (BS3) (Sigma-Aldrich), with a spacer arm of 11.4 Å between their Cα carbons, on ice for 2 hours. The reaction was terminated by applying 50 mM tris-HCl (pH 7.5) at room temperature for 15 min. Cross-linked complexes were precipitated and digested using trypsin for 16 hours at 37°C at an enzyme-to-substrate ratio of 1:50 (w/w). The tryptic-digested peptides were desalted and loaded on an in-house packed capillary reverse-phase S18 column (40 cm in length, 100-μm inner diameter by 360-μm outer diameter, 1.9 μm of particle size, 120 Å of pore diameter) connected to an Easy LC 1200 system. The samples were analyzed with a 120-min high-performance liquid chromatography gradient from 6 to 35% of buffer B (buffer A: 0.1% formic acid in water; buffer B: 0.1% formic acid in 80% acetonitrile) at 300 nl/min. The eluted peptides were ionized and directly introduced into a Q Exactive mass spectrometer using a nanospray source. Survey full-scan MS spectra [from mass/charge ratio (m/z) of 300 to 1800] were acquired using an Orbitrap analyzer with a resolution $r = 70{,}000$ at m/z 400. Cross-linked peptides were identified and evaluated using pLink2 software (*59*).

Cryo-EM sample preparation and data acquisition

To prepare a vitreous sample of the TRiC-plp2-actin complex without addition of nucleotide or vitreous samples of TRiC-plp2-actin and TRiC-actin complexes in the presence of ATP-AlFx, respectively, in each case, an aliquot of 2.2-μl biological sample obtained using an abovementioned producer was applied to a glow-discharged holey carbon grid (R1.2/1.3, 200 mesh; Quantifoil). The grid was blotted with Vitrobot Mark IV (Thermo Fisher Scientific) and then plunged into liquid ethane cooled by liquid nitrogen. To handle the preferred orientation problem, the grid was pretreated with polylysine (*18*).

For each of the experimental sample conditions mentioned above, cryo-EM movies of the sample were collected using a Titan Krios electron microscope equipped with a Cs corrector (Thermo Fisher Scientific) operated at an accelerating voltage of 300 kV with a nominal magnification of ×18,000 (table S1). The movies were recorded using a K2 Summit direct electron detector (Gatan) operated in super-resolution mode (yielding a pixel size of 1.318 Å after two times binning) under a low-dose condition in an automatic manner using SerialEM (*60*). Each frame was exposed for 0.2 s, and the total accumulation time was 7.6 s, leading to a total accumulated dose of 38 $e^-/Å^2$ on the specimen.

Image processing and 3D reconstruction

The image processing and reconstruction procedures are shown in figs. S3, S4, and S7 and table S1. For the TRiC-plp2-actin sample, the motion correction of each movie stack was performed using the Motioncorr2 program (*61*) before further image processing. The contrast transfer function (CTF) parameters of each image were determined using CTFFIND4 (*62*). About 1000 particles were manually picked and then subjected to 2D classification using Relion 3.1, after which several good class averages were chosen as templates for further automatic particle picking in Relion3.1 (*63*). Bad particles and ice contaminations were then excluded by performing manual selection and 2D classification. Then, 513,339 particles were refined and re-extracted to recenter against a previously determined TRiC map, which was low-pass-filtered to 20 Å. No symmetry was imposed in our procedure.

We first 3D classified the entire dataset into six classes: the last two classes presented better structural features (than did the other four classes), and the remaining four classes were combined for another round of 3D classification, generating six classes, four of which showed better structural features and were combined for another round of 2D classification. Then, the selected particles were combined with the previous good particles, after which CTF refinement and per-particle motion correction (also known as Bayesian polishing) were performed using Relion3.1. We then masked extra pieces of density out and subtracted particles for two rounds of focused 3D classification. Then, 50,513 particles showing improved extra pieces of density were selected for the final reconstruction to 4.55 Å. The resolution estimation was based on the gold-standard criterion using a Fourier shell correlation (FSC) of 0.143, and the local resolution was estimated using ResMap (*25*).

Procedures similar to those described above were used for the cryo-EM samples of the TRiC-plp2-actin complex with ATP-AlFx, with the details provided in fig. S4 and table S1. Moreover, for the dataset of the open-state species, after having obtained a 3.78-Å-resolution map, we also applied a focused 3D classification on the extra density of the cis-/trans-ring. Here, 33,866 particles were reconstructed to a final 3.91-Å-resolution map with extra pieces of density in both rings. For the dataset of the closed-state species, after having obtained a 2.97-Å-resolution map using the abovementioned procedure, we masked extra pieces of density out and subtracted particles for focused 3D classification. Two new classes had different pieces of density in both rings and included 10.30 and 12.38% of the particles; while the majority of the particles (69.67%) had the same conformation in both rings. Then, we reverted the two new classes to the original particles for refinement. For an exhaustive classification of the extra density, we subtracted the cis-ring and trans-ring from the closed TRiC particles, respectively. We then applied focused 3D classification with different masks on cis-ring or trans-ring particles. By combining the cis-ring–classified and trans-ring–classified particles and taking the intersection of these classes (with squares in different color shades in fig. S4 representing the selected intersection in similar condition), three new conformations with distinct extra pieces of density in the trans-ring were resolved at 3.39, 3.20, and 3.05 Å and termed as S3, S4, and S5 states, respectively. The resolution estimation was based on the gold-standard criterion using an FSC of 0.143, and the local resolution was estimated using ResMap (*64*).

For the TRiC-actin dataset (see fig. S7), 94,912 particles remained after 2D classification. After several rounds of 2D/3D classification, 17,156 particles in the closed state of TRiC were selected and loaded into cryoSPARC V3.3.1 (*65*) and were refined to 3.87-Å resolution, using nonuniform refinement. The overall resolution was determined based on the gold-standard criterion using an FSC of 0.143.

Atomic model building by flexible fitting

We built atomic models for the better resolved S1, S2, S3, S4, and S5 maps. TRiC-NPP [Protein Data Bank (PDB): 5GW4], TRiC-AMP-PNP (PDB: 5GW5), and closed-state TRiC (PDB: 6KS6) complexes, which were conformationally similar to our current structures, were used as the initial models. Then, the models for the subunits were fitted into the density map simultaneously as rigid body using UCSF Chimera and were combined as a complete model (*66*). Then, we used phenix.real_space_refine to improve the fitting (*67*). We also performed real-space refinement using COOT (*68*) to eliminate steric clashes and, in the last round, performed flexible fitting on the entire complex using Rosetta followed by Phenix (*69*).

For the plp2 initial model used in S3, S4, and S5, we first chose the complete model of yeast plp2 from the AlphaFold database (*70*). After carrying out rigid-body docking of this model, we performed a flexible fitting of each of the domains using phenix.real_space_refine and one more round of flexible fitting using Rosetta. Last, we performed real-space refinement using COOT to eliminate steric clashes and performed the last round of flexible fitting of plp2 using Rosetta followed by Phenix.

For the tubulin model in S3, we first chose the complete model of yeast β-tubulin (PDB: 5W3F) as the initial model. After rigid-body docking, we performed flexible fitting of each of the domains using phenix.real_space_refine and one more round of flexible fitting using Rosetta. Last, we performed real-space refinement using COOT to eliminate steric clashes and performed the last round of flexible fitting of tubulin using Rosetta followed by Phenix.

ATPase activity assay

ATP hydrolysis rates of TRiC with plp2 and β-actin were measured by performing an NADH-coupled assay (*71*). In this assay, each ATP hydrolysis event allows conversion of one molecule of phosphoenolpyruvate into pyruvate by pyruvate kinase. Thereafter, pyruvate was converted to lactate as catalyzed by L-lactate dehydrogenase, which resulted in oxidation of a single NADH molecule. Loss of NADH over time, which was quantifiably proportional to the ATP hydrolysis rate, was monitored by measuring the decrease in absorbance at 340 nm. All the assays were conducted at 30°C in a buffer containing 10 mM Mops-KOH (pH 8.0), 20 mM KCl, and 10 mM $MgCl_2$ and in the presence of 1 mM ATP. Experiments were performed in triplicate using 1 μM of the protein complex. Absorbance was measured in a 100-μl reaction volume using a 96-well plate reader. Data analysis was performed using GraphPad Prism 8.

Thermal stability measurements

To determine the thermal stability of plp2 and β-actin, solutions of proteins alone or pretreated with 2 mM EDTA were administered into respective capillary tubes, which were then placed into a Prometheus apparatus (NanoTemper) for measuring thermal stability. Meanwhile, we used α-actin from rabbit muscle (Sigma-Aldrich) as a control. The temperature was increased at a rate of 2.0°C/min until 95°C. Then, thermal stability curves were drawn with the temperature on the *x* axis and first derivative of the ratio between integrated fluorescence at 350 nm and that at 330 nm on the *y* axis. Each experiment was repeated three times.

Supplementary Materials

This PDF file includes:
Figs. S1 to S7
Tables S1 to S5
Legend for movie S1
References

Other Supplementary Material for this manuscript includes the following:
Movie S1

View/request a protocol for this paper from *Bio-protocol*.

REFERENCES AND NOTES

1. L. Chen, Z. Zhang, J. Qiu, L. Zhang, X. Luo, J. Jang, Chaperonin CCT-mediated AIB1 folding promotes the growth of ERα-positive breast cancer cells on hard substrates. *PLOS ONE* **9**, e96085 (2014).
2. R. Bassiouni, K. N. Nemec, A. Iketani, O. Flores, A. Showalter, A. S. Khaled, P. Vishnubhotla, R. W. Sprung Jr., C. Kaittanis, J. M. Perez, A. R. Khaled, Chaperonin containing TCP-1 protein level in breast cancer cells predicts therapeutic application of a cytotoxic peptide. *Clin. Cancer Res.* **22**, 4366–4379 (2016).
3. M. Jin, C. Liu, W. Han, Y. Cong, TRiC/CCT chaperonin: Structure and function. *Subcell. Biochem.* **93**, 625–654 (2019).
4. R. Melki, N. J. Cowan, Facilitated folding of actins and tubulins occurs via a nucleotide-dependent interaction between cytoplasmic chaperonin and distinctive folding intermediates. *Mol. Cell. Biol.* **14**, 2895–2904 (1994).
5. D. B. Vinh, D. G. Drubin, A yeast TCP-1-like protein is required for actin function in vivo. *Proc. Natl. Acad. Sci. U.S.A.* **91**, 9116–9120 (1994).
6. O. Llorca, J. Martín-Benito, M. Ritco-Vonsovici, J. Grantham, G. M. Hynes, K. R. Willison, J. L. Carrascosa, J. M. Valpuesta, Eukaryotic chaperonin CCT stabilizes actin and tubulin folding intermediates in open quasi-native conformations. *EMBO J.* **19**, 5971–5979 (2000).
7. O. Llorca, J. Martín-Benito, J. Grantham, M. Ritco-Vonsovici, K. R. Willison, J. L. Carrascosa, J. M. Valpuesta, The 'sequential allosteric ring' mechanism in the eukaryotic chaperonin-assisted folding of actin and tubulin. *EMBO J.* **20**, 4065–4075 (2001).
8. A. Camasses, A. Bogdanova, A. Shevchenko, W. Zachariae, The CCT chaperonin promotes activation of the anaphase-promoting complex through the generation of functional Cdc20. *Mol. Cell* **12**, 87–100 (2003).
9. A. G. Trinidad, P. A. J. Muller, J. Cuellar, M. Klejnot, M. Nobis, J. M. Valpuesta, K. H. Vousden, Interaction of p53 with the CCT complex promotes protein folding and wild-type p53 activity. *Mol. Cell* **50**, 805–817 (2013).
10. M. Kasembeli, W. C. Y. Lau, S. H. Roh, T. K. Eckols, J. Frydman, W. Chiu, D. J. Tweardy, Modulation of STAT3 folding and function by TRiC/CCT chaperonin. *PLOS Biol.* **12**, e1001844 (2014).
11. A. J. McClellan, M. D. Scott, J. Frydman, Folding and quality control of the VHL tumor suppressor proceed through distinct chaperone pathways. *Cell* **121**, 739–748 (2005).
12. Y. Cong, G. F. Schröder, A. S. Meyer, J. Jakana, B. Ma, M. T. Dougherty, M. F. Schmid, S. Reissmann, M. Levitt, S. L. Ludtke, J. Frydman, W. Chiu, Symmetry-free cryo-EM structures of the chaperonin TRiC along its ATPase-driven conformational cycle. *EMBO J.* **31**, 720–730 (2012).
13. A. S. Meyer, J. R. Gillespie, D. Walther, I. S. Millet, S. Doniach, J. Frydman, Closing the folding chamber of the eukaryotic chaperonin requires the transition state of ATP hydrolysis. *Cell* **113**, 369–381 (2003).
14. C. Spiess, A. S. Meyer, S. Reissmann, J. Frydman, Mechanism of the eukaryotic chaperonin: Protein folding in the chamber of secrets. *Trends Cell Biol.* **14**, 598–604 (2004).
15. M. Jin, W. Han, C. Liu, Y. Zang, J. Li, F. Wang, Y. Wang, Y. Cong, An ensemble of cryo-EM structures of TRiC reveal its conformational landscape and subunit specificity. *Proc. Natl. Acad. Sci. U.S.A.* **116**, 19513–19522 (2019).
16. N. Kalisman, C. M. Adams, M. Levitt, Subunit order of eukaryotic TRiC/CCT chaperonin by cross-linking, mass spectrometry, and combinatorial homology modeling. *Proc. Natl. Acad. Sci. U.S.A.* **109**, 2884–2889 (2012).
17. H. Wang, W. Han, J. Takagi, Y. Cong, Yeast inner-subunit PA–NZ-1 labeling strategy for accurate subunit identification in a macromolecular complex through cryo-EM analysis. *J. Mol. Biol.* **430**, 1417–1425 (2018).
18. Y. Zang, M. Jin, H. Wang, Z. Cui, L. Kong, C. Liu, Y. Cong, Staggered ATP binding mechanism of eukaryotic chaperonin TRiC (CCT) revealed through high-resolution cryo-EM. *Nat. Struct. Mol. Biol.* **23**, 1083–1091 (2016).

19. Y. Zang, H. Wang, Z. Cui, M. Jin, C. Liu, W. Han, Y. Wang, Y. Cong, Development of a yeast internal-subunit eGFP labeling strategy and its application in subunit identification in eukaryotic group II chaperonin TRiC/CCT. *Sci. Rep.* **8**, 2374 (2018).
20. A. Leitner, L. A. Joachimiak, A. Bracher, L. Mönkemeyer, T. Walzthoeni, B. Chen, S. Pechmann, S. Holmes, Y. Cong, B. Ma, S. Ludtke, W. Chiu, F. U. Hartl, R. Aebersold, J. Frydman, The molecular architecture of the eukaryotic chaperonin TRiC/CCT. *Structure* **20**, 814–825 (2012).
21. S. Reissmann, L. A. Joachimiak, B. Chen, A. S. Meyer, A. Nguyen, J. Frydman, A gradient of ATP affinities generates an asymmetric power stroke driving the chaperonin TRIC/CCT folding cycle. *Cell Rep.* **2**, 866–877 (2012).
22. L. Ditzel, J. Löwe, D. Stock, K. O. Stetter, H. Huber, R. Huber, S. Steinbacher, Crystal structure of the thermosome, the archaeal chaperonin and homolog of CCT. *Cell* **93**, 125–138 (1998).
23. T. Waldmann, A. Lupas, J. Kellermann, J. Peters, W. Baumeister, Primary structure of the thermosome from Thermoplasma acidophilum. *Biol. Chem. Hoppe Seyler* **376**, 119–126 (1995).
24. M. Klumpp, W. Baumeister, L. O. Essen, Structure of the substrate binding domain of the thermosome, an archaeal group II chaperonin. *Cell* **91**, 263–270 (1997).
25. V. F. Lundin, M. R. Leroux, P. C. Stirling, Quality control of cytoskeletal proteins and human disease. *Trends Biochem. Sci.* **35**, 288–297 (2010).
26. I. E. Vainberg, S. A. Lewis, H. Rommelaere, C. Ampe, J. Vandekerckhove, H. L. Klein, N. J. Cowan, Prefoldin, a chaperone that delivers unfolded proteins to cytosolic chaperonin. *Cell* **93**, 863–873 (1998).
27. S. Geissler, K. Siegers, E. Schiebel, A novel protein complex promoting formation of functional alpha- and gamma-tubulin. *EMBO J.* **17**, 952–966 (1998).
28. J. J. Knowlton, D. Gestaut, B. Ma, G. Taylor, A. B. Seven, A. Leitner, G. J. Wilson, S. Shanker, N. A. Yates, B. V. V. Prasad, R. Aebersold, W. Chiu, J. Frydman, T. S. Dermody, Structural and functional dissection of reovirus capsid folding and assembly by the prefoldin-TRiC/CCT chaperone network. *Proc. Natl. Acad. Sci. U.S.A.* **118**, e2018127118 (2021).
29. D. Gestaut, Y. Zhao, J. Park, B. Ma, A. Leitner, M. Collier, G. Pintilie, S.-H. Roh, W. Chiu, J. Frydman, Structural visualization of the tubulin folding pathway directed by eukaryotic chaperonin TRiC. *bioRxiv* 2022.03.25.483853 [Preprint] 26 March 2022. https://doi.org/10.1101/2022.03.25.483853.
30. K. Siegers, T. Waldmann, M. R. Leroux, K. Grein, A. Shevchenko, E. Schiebel, F. U. Hartl, Compartmentation of protein folding in vivo: sequestration of non-native polypeptide by the chaperonin-GimC system. *EMBO J.* **18**, 75–84 (1999).
31. R. Siegert, M. R. Leroux, C. Scheufler, F. U. Hartl, I. Moarefi, Structure of the molecular chaperone prefoldin: Unique interaction of multiple coiled coil tentacles with unfolded proteins. *Cell* **103**, 621–632 (2000).
32. B. M. Willardson, A. C. Howlett, Function of phosducin-like proteins in G protein signaling and chaperone-assisted protein folding. *Cell. Signal.* **19**, 2417–2427 (2007).
33. P. C. Stirling, J. Cuéllar, G. A. Alfaro, F. el Khadali, C. T. Beh, J. M. Valpuesta, R. Melki, M. R. Leroux, PhLP3 modulates CCT-mediated actin and tubulin folding via ternary complexes with substrates. *J. Biol. Chem.* **281**, 7012–7021 (2006).
34. C. Bregier, L. KrzemieŃ-Ojak, D. WŁOga, M. Jerka-Dziadosz, E. Joachimiak, K. Batko, I. Filipiuk, U. ŚMietanka, J. Gaertig, S. Ł. A. Fabczak, H. Fabczak, PHLP2 is essential and plays a role in ciliogenesis and microtubule assembly in Tetrahymena thermophila. *J. Cell. Physiol.* **228**, 2175–2189 (2013).
35. P. C. Stirling, M. Srayko, K. S. Takhar, A. Pozniakovsky, A. A. Hyman, M. R. Leroux, Functional interaction between phosducin-like protein 2 and cytosolic chaperonin is essential for cytoskeletal protein function and cell cycle progression. *Mol. Biol. Cell* **18**, 2336–2345 (2007).
36. E. A. McCormack, G. M. Altschuler, C. Dekker, H. Filmore, K. R. Willison, Yeast phosducin-like protein 2 acts as a stimulatory co-factor for the folding of actin by the chaperonin CCT via a ternary complex. *J. Mol. Biol.* **391**, 192–206 (2009).
37. S. F. Stuart, R. J. Leatherbarrow, K. R. Willison, A two-step mechanism for the folding of actin by the yeast cytosolic chaperonin. *J. Biol. Chem.* **286**, 178–184 (2011).
38. K. R. Willison, The structure and evolution of eukaryotic chaperonin-containing TCP-1 and its mechanism that folds actin into a protein spring. *Biochem. J.* **475**, 3009–3034 (2018).
39. D. Balchin, G. Milicic, M. Strauss, M. Hayer-Hartl, F. U. Hartl, Pathway of actin folding directed by the eukaryotic chaperonin TRiC. *Cell* **174**, 1507–1521.e16 (2018).
40. I. G. Munoz, H. Yébenes, M. Zhou, P. Mesa, M. Serna, A. Y. Park, E. Bragado-Nilsson, A. Beloso, G. de Cárcer, M. Malumbres, C. V. Robinson, J. M. Valpuesta, G. Montoya, Crystal structure of the open conformation of the mammalian chaperonin CCT in complex with tubulin. *Nat. Struct. Mol. Biol.* **18**, 14–19 (2011).
41. C. Dekker, S. M. Roe, E. A. McCormack, F. Beuron, L. H. Pearl, K. R. Willison, The crystal structure of yeast CCT reveals intrinsic asymmetry of eukaryotic cytosolic chaperonins. *EMBO J.* **30**, 3078–3090 (2011).
42. O. Llorca, E. A. McCormack, G. Hynes, J. Grantham, J. Cordell, J. L. Carrascosa, K. R. Willison, J. J. Fernandez, J. M. Valpuesta, Eukaryotic type II chaperonin CCT interacts with actin through specific subunits. *Nature* **402**, 693–696 (1999).
43. J. J. Kelly, D. Tranter, E. Pardon, G. Chi, H. Kramer, L. Happonen, K. M. Knee, J. M. Janz, J. Steyaert, C. Bulawa, V. O. Paavilainen, J. T. Huiskonen, W. W. Yue, Snapshots of actin and tubulin folding inside the TRiC chaperonin. *Nat. Struct. Mol. Biol.* **29**, 420–429 (2022).
44. D. Gestaut, S. H. Roh, B. Ma, G. Pintilie, L. A. Joachimiak, A. Leitner, T. Walzthoeni, R. Aebersold, W. Chiu, J. Frydman, The chaperonin TRiC/CCT associates with prefoldin through a conserved electrostatic interface essential for cellular proteostasis. *Cell* **177**, 751–765.e15 (2019).
45. C. R. Booth, A. S. Meyer, Y. Cong, M. Topf, A. Sali, S. J. Ludtke, W. Chiu, J. Frydman, Mechanism of lid closure in the eukaryotic chaperonin TRiC/CCT. *Nat. Struct. Mol. Biol.* **15**, 746–753 (2008).
46. Y. Cong, M. L. Baker, J. Jakana, D. Woolford, E. J. Miller, S. Reissmann, R. N. Kumar, A. M. Redding-Johanson, T. S. Batth, A. Mukhopadhyay, S. J. Ludtke, J. Frydman, W. Chiu, 4.0-A resolution cryo-EM structure of the mammalian chaperonin TRiC/CCT reveals its unique subunit arrangement. *Proc. Nat. Acad. Sci. U.S.A* **107**, 4967–4972 (2010).
47. E. Nogales, S. G. Wolf, K. H. Downing, Structure of the alpha beta tubulin dimer by electron crystallography. *Nature* **391**, 199–203 (1998).
48. J. Lowe, H. Li, K. H. Downing, E. Nogales, Refined structure of alpha beta-tubulin at 3.5 A resolution. *J. Mol. Biol* **313**, 1045–1057 (2001).
49. K. I. Brackley, J. Grantham, Activities of the chaperonin containing TCP-1 (CCT): Implications for cell cycle progression and cytoskeletal organisation. *Cell Stress Chaperones* **14**, 23–31 (2009).
50. G. W. Farr, E. C. Scharl, R. J. Schumacher, S. Sondek, A. L. Horwich, Chaperonin-mediated folding in the eukaryotic cytosol proceeds through rounds of release of native and non-native forms. *Cell* **89**, 927–937 (1997).
51. R. L. Plimpton, J. Cuéllar, C. W. J. Lai, T. Aoba, A. Makaju, S. Franklin, A. D. Mathis, J. T. Prince, J. L. Carrascosa, J. M. Valpuesta, B. M. Willardson, Structures of the Gβ-CCT and PhLP1–Gβ-CCT complexes reveal a mechanism for G-protein β-subunit folding and Gβγ dimer assembly. *Proc. Natl. Acad. Sci. U.S.A.* **112**, 2413–2418 (2015).
52. S. H. Roh, M. M. Kasembeli, J. G. Galaz-Montoya, W. Chiu, D. J. Tweardy, Chaperonin TRiC/CCT recognizes fusion oncoprotein AML1-ETO through subunit-specific interactions. *Biophys. J.* **110**, 2377–2385 (2016).
53. J. Cuellar, W. G. Ludlam, N. C. Tensmeyer, T. Aoba, M. Dhavale, C. Santiago, M. T. Bueno-Carrasco, M. J. Mann, R. L. Plimpton, A. Makaju, S. Franklin, B. M. Willardson, J. M. Valpuesta, Structural and functional analysis of the role of the chaperonin CCT in mTOR complex assembly. *Nat. Commun.* **10**, 2865 (2019).
54. J. Cuellar, J. Martín-Benito, S. H. W. Scheres, R. Sousa, F. Moro, E. López-Viñas, P. Gómez-Puertas, A. Muga, J. L. Carrascosa, J. M. Valpuesta, The structure of CCT-Hsc70 NBD suggests a mechanism for Hsp70 delivery of substrates to the chaperonin. *Nat. Struct. Mol. Biol.* **15**, 858–864 (2008).
55. J. Martin-Benito, S. Bertrand, T. Hu, P. J. Ludtke, J. N. McLaughlin, B. M. Willardson, J. L. Carrascosa, J. M. Valpuesta, Structure of the complex between the cytosolic chaperonin CCT and phosducin-like protein. *Proc. Natl. Acad. Sci. U.S.A.* **101**, 17410–17415 (2004).
56. J. Martin-Benito, J. Boskovic, P. Gómez-Puertas, J. L. Carrascosa, C. T. Simons, S. A. Lewis, F. Bartolini, N. J. Cowan, J. M. Valpuesta, Structure of eukaryotic prefoldin and of its complexes with unfolded actin and the cytosolic chaperonin CCT. *EMBO J.* **21**, 6377–6386 (2002).
57. M. Jin, Y. Cong, Identification of an allosteric network that influences assembly and function of group II chaperonins. *Nat. Struct. Mol. Biol.* **24**, 683–684 (2017).
58. T. Lopez, K. Dalton, A. Tomlinson, V. Pande, J. Frydman, An information theoretic framework reveals a tunable allosteric network in group II chaperonins. *Nat. Struct. Mol. Biol.* **24**, 726–733 (2017).
59. S. Lu, S. B. Fan, B. Yang, Y. X. Li, J. M. Meng, L. Wu, P. Li, K. Zhang, M. J. Zhang, Y. Fu, J. Luo, R. X. Sun, S. M. He, M. Q. Dong, Mapping native disulfide bonds at a proteome scale. *Nat. Methods* **12**, 329–331 (2015).
60. D. N. Mastronarde, Automated electron microscope tomography using robust prediction of specimen movements. *J. Struct. Biol.* **152**, 36–51 (2005).
61. S. Q. Zheng, E. Palovcak, J. P. Armache, K. A. Verba, Y. Cheng, D. A. Agard, MotionCor2: Anisotropic correction of beam-induced motion for improved cryo-electron microscopy. *Nat. Methods* **14**, 331–332 (2017).
62. A. Rohou, N. Grigorieff, CTFFIND4: Fast and accurate defocus estimation from electron micrographs. *J. Struct. Biol.* **192**, 216–221 (2015).
63. J. Zivanov, T. Nakane, B. O. Forsberg, D. Kimanius, W. J. H. Hagen, E. Lindahl, S. H. W. Scheres, New tools for automated high-resolution cryo-EM structure determination in RELION-3. *eLife* **7**, e42166 (2018).
64. A. Kucukelbir, F. J. Sigworth, H. D. Tagare, Quantifying the local resolution of cryo-EM density maps. *Nat. Methods* **11**, 63–65 (2014).

65. A. Punjani, J. L. Rubinstein, D. J. Fleet, M. A. Brubaker, cryoSPARC: Algorithms for rapid unsupervised cryo-EM structure determination. *Nat. Methods* **14**, 290–296 (2017).
66. Z. Yang, K. Lasker, D. Schneidman-Duhovny, B. Webb, C. C. Huang, E. F. Pettersen, T. D. Goddard, E. C. Meng, A. Sali, T. E. Ferrin, UCSF Chimera, MODELLER, and IMP: an integrated modeling system. *J. Struct. Biol.* **179**, 269–278 (2012).
67. P. D. Adams, P. V. Afonine, G. Bunkóczi, V. B. Chen, I. W. Davis, N. Echols, J. J. Headd, L. W. Hung, G. J. Kapral, R. W. Grosse-Kunstleve, A. J. McCoy, N. W. Moriarty, R. Oeffner, R. J. Read, D. C. Richardson, J. S. Richardson, T. C. Terwilliger, P. H. Zwart, PHENIX: A comprehensive Python-based system for macromolecular structure solution. *Acta Crystallogr. D Biol. Crystallogr.* **66**, 213–221 (2010).
68. P. Emsley, K. Cowtan, Coot: Model-building tools for molecular graphics. *Acta Crystallogr. D Biol. Crystallogr.* **60**, 2126–2132 (2004).
69. R. Y. Wang, Y. Song, B. A. Barad, Y. Cheng, J. S. Fraser, F. D. Maio, Automated structure refinement of macromolecular assemblies from cryo-EM maps using Rosetta. *eLife* **5**, e17219 (2016).
70. J. Jumper, R. Evans, A. Pritzel, T. Green, M. Figurnov, O. Ronneberger, K. Tunyasuvunakool, R. Bates, A. Žídek, A. Potapenko, A. Bridgland, C. Meyer, S. A. A. Kohl, A. J. Ballard, A. Cowie, B. Romera-Paredes, S. Nikolov, R. Jain, J. Adler, T. Back, S. Petersen, D. Reiman, E. Clancy, M. Zielinski, M. Steinegger, M. Pacholska, T. Berghammer, S. Bodenstein, D. Silver, O. Vinyals, A. W. Senior, K. Kavukcuoglu, P. Kohli, D. Hassabis, Highly accurate protein structure prediction with AlphaFold. *Nature* **596**, 583–589 (2021).
71. J. G. Norby, Coupled assay of Na+,K+-ATPase activity. *Methods Enzymol.* **156**, 116–119 (1988).
72. M. W. Melville, A. J. McClellan, A. S. Meyer, A. Darveau, J. Frydman, The Hsp70 and TRiC/CCT chaperone systems cooperate in vivo to assemble the von Hippel-Lindau tumor suppressor complex. *Mol. Cell. Biol.* **23**, 3141–3151 (2003).

Acknowledgments: We are grateful to the staffs of the NCPSS Electron Microscopy facility, Database and Computing facility, Protein Expression and Purification facility, and Mass Spectrometry facility for instrument support and technical assistance. **Funding:** This work was supported by grants from the Strategic Priority Research Program of CAS (XDB37040103), the NSFC (32130056 and 31872714), National Key R&D Program of China (2017YFA0503503), Shanghai Academic Research Leader (20XD1404200), and Shanghai Pilot Program for Basic Research from CAS (JCYJ-SHFY-2022-008). **Author contributions:** W.H., M.J., and Y.C. designed the experiments. W.H. and M.J. purified the proteins, prepared the sample, and collected the cryo-EM data. W.H., Yifan Wang, and C.L. performed data reconstruction. W.H. performed model building. W.H., Q.Z., S.W., and Yanxing Wang performed the biochemistry experiments. C.P. and Y.Y. performed the XL-MS experiments and data analysis. W.H. and Y.C. analyzed the data and wrote the manuscript. **Competing interests:** The authors declare that they have no competing interests. **Data and materials availability:** All data needed to evaluate the conclusions in the paper are present in the paper and/or the Supplementary Materials. Cryo-EM maps determined for the TRiC-plp2-substrate complexes (S1 to S5) have been deposited at the Electron Microscopy Data Bank with accession codes EMD-33917, EMD-33918, EMD-33919, EMD-33920, and EMD-33921, and the associated atomic models have been deposited in the Protein Data Bank with accession codes 7YLU, 7YLV, 7YLW, 7YLX, and 7YLY.

Submitted 27 July 2022
Accepted 14 February 2023
Published 15 March 2023
10.1126/sciadv.ade1207